

Unraveling materials Berry curvature and Chern-Simons numbers from real-time evolution of Bloch states

Dongbin Shin¹, Shunsuke A. Sato², Hannes Hübenner², Umberto De Giovannini², Jeongwoo Kim¹, Angel Rubio^{2,3,4,}, Noejung Park^{1,2,*}*

¹*Department of Physics, Ulsan National Institute of Science and Technology, Ulsan, 689-798 Korea*

²*Max Planck Institute for the Structure and Dynamics of Matter, Luruper Chaussee 149, 22761 Hamburg, Germany*

³*Center for Computational Quantum Physics (CCQ), The Flatiron Institute, 162 Fifth Avenue, New York NY 10010*

⁴*Nano-Bio Spectroscopy Group, Departamento de Física de Materiales, Universidad del País Vasco UPV/EHU, 20018 San Sebastián, Spain*

Subject Areas: Computational Physics, Condensed Matter Physics, Materials Science

Materials can be classified by the topological character of their electronic structure and, in this perspective, global attributes immune to local deformations have been discussed in terms of Berry curvature and Chern numbers. Except for instructional simple models, linear response theories have been ubiquitously employed in calculations of topological properties of real materials. Here we propose a completely different and versatile approach to get the topological characteristics of materials by calculating physical observables from the real-time evolving Bloch states: the cell-averaged current density reveals the anomalous velocities whose

integration leads to the conductivity quantum. Results for prototypical cases are shown, including a spin-frozen valley-Hall and a quantum anomalous Hall insulator. The advantage of this method is best illustrated by the example of a quantum spin Hall insulator: the quantized spin Hall conductivity is straightforwardly obtained irrespective of the non-Abelian nature in its Berry curvature. Moreover, the method can be extended to the description of real observables in non-equilibrium states of topological materials.

I. INTRODUCTION

When the Hamiltonian of a system is subject to adjustable periodic parameters, the eigenstates can acquire a nontrivial gauge-independent phase over the adiabatic evolution in the parameter space [1,2]. In various areas of physics the presence and importance of such geometrical phases have been recognized and characterized through the formulation owed to Chern-Simons and Berry [1,3,4]. In particular, the geometrical phase resulting from a variation of the Bloch vector (\vec{k}) of a periodic Hamiltonian ($\hat{H}(\vec{k}) = e^{-i\vec{k}\cdot\vec{r}} \hat{H} e^{i\vec{k}\cdot\vec{r}}$) has recently attracted the most attention in the condensed matter community [5-7]. This Bloch geometrical property can also be discussed by a local field, known as Berry curvature ($\Omega(\vec{k})$), defined on the parameter space [2], instead of the loop-integrated phase. Once a finite Berry curvature is present, a solid will get an intrinsic anomalous Hall conductivity and, in this regard, the Berry curvature can be thought of as an intrinsic magnetic field of the material [2,6,8,9]. Furthermore, as established by Chern and Simons [4], the integration of the Berry curvature over a closed surface is quantized, named as Chern integer, which has been recognized as an essential indicator of the band topological nature [3]. For example, for two-dimensional (2D) Bloch electrons, the Chern number n can be determined by the integration over the whole Brillouin

$$\text{Zone (BZ): } n = \frac{1}{2\pi} \int_{\text{BZ}} \Omega(k_x, k_y) d^2k .$$

In addition to the anomalous charge Hall conductivity, various other transport properties can reflect the effects of the Berry curvature, such as, the valley Hall or spin Hall effect and others [9-12]. Except for instructionally designed simple models, the calculation of Berry curvature and the Chern-Simons number for real materials requisitely involves a perturbative approach within linear response theory, which in most cases requires the Wannierization technique to cope with the fine-grid integral over the BZ [13-15]. In the linear responses formulation, a monochromatic field ($\vec{E}_{ext} e^{i\omega t}$) is introduced to perturb the ground state, and the off-diagonal element ($\sigma_{xy}(\omega)$) of the conductivity tensor $\sigma(\omega)$ is written in terms of the unperturbed eigenstates, by means of the Kubo formula [2,10]. In particular, the static Hall conductivity ($\sigma_{xy}(\omega \rightarrow 0)$) has been assigned the most significant physical meaning owing to the work of Thouless, Kohmoto, Nightingale and Nijs (TKNN): the quantized Hall conductivity of the Landau level insulator is exactly related to the integer indicator of the topology (n as $\sigma_{xy} = ne^2/h$) [3]. The intrinsic Chern number n of a material, as opposed to that of a quantum Hall state formed by an external magnetic field, was pursued in the search for quantum anomalous phases [16], and Haldane's suggestion for the spin-frozen Chern insulator ignited flourishing interest toward topological states of matter [17]: Kane and Mele suggested the topological quantum spin Hall (QSH) effect by considering two copies of Haldane's model, constituting the time-reversal partner to each other [18,19]. Bernevig, Hughes, and Zhang presented the same concept of a QSH effect through the exploration of an intrinsically band-inverted semiconductor and its surface state [20,21]. Extension to three dimensions (3D) and the relevant topological numbers have been pursued, and the

topologically protected metallic surface bands at the boundary of distinct topological states have been observed and discussed in the perspectives of spin-resolved dissipation-less carrier transport [5,22-24]. More comprehensive overviews of the topological phases of materials, and their historical developments, have been provided in a few recent review articles [2,5,24].

This work is motivated by the question of whether the Berry curvature can be extracted from physical observables, such as the total current or others, that can be obtained from the time evolving states of a solid ($\psi_{n,k}(t)$) through the time-dependent Schrödinger equation. For actual time propagation, in the present work, we perform first-principles time-dependent density functional theory (TDDFT) calculations, and we show that the Berry curvature and Chern-Simons numbers for bands can be obtained from the time profiles of the total current. This method does not require the commonly used Wannierization technique, and physical observables (charge or spin current) are directly computed as expectation values from the time-evolving solid states. Exemplary real-material systems are presented including a trivial insulator, a valley-Hall insulator, and a quantum anomalous Hall insulator (QAHI). Using an example of a quantum spin Hall insulator (QSHI) we explicitly demonstrate that this dynamical approach offers a natural standpoint for spin Hall conductivity when the Berry curvature is non-Abelian and thus gauge-dependent.

II. THEORETICAL FRAMEWORK AND COMPUTATION METHOD

The computation method consists in the use of a spatially uniform electric field (E-field) in the form of a time-dependent vector potential: $\vec{A}(t) = -c \int_{-\infty}^t \vec{E}(\tau) d\tau$. Time-evolving solid state wavefunctions are computed through the time-dependent Kohn-Sham (KS) equation, as

derived within TDDFT [25,26],

$$i\hbar \frac{\partial}{\partial t} |\psi_{n,\bar{k}}(t)\rangle = \left[\frac{1}{2m} \left(-i\hbar \vec{\nabla} + \frac{e}{c} \vec{A}(t) \right)^2 + \hat{V}_{ext}(\vec{r}) + V_{Hxc}[\rho(\vec{r},t)] + \hat{V}_{SOC} \right] |\psi_{n,\bar{k}}(t)\rangle, \quad (1)$$

where $\hat{V}_{ext}(\vec{r})$ indicates the scalar-type external potential including atomic pseudopotential; and $V_{Hxc}[\rho]$ and \hat{V}_{SOC} are Hartree-exchange-correlation density-functional potentials and the spin-orbit coupling term, respectively. The Kohn-Sham wavefunctions $|\psi_{n,\bar{k}}(t)\rangle$ are two-component spinors or a single-component wavefunctions (the spin-frozen or spin-polarized ones). Detailed parameters related to standard DFT calculation [27] and the time-integration algorithms are described in the Appendix A.

Once the time-evolving solid states ($|\psi_{n,\bar{k}}(t)\rangle$) are computed the expectation values of an observable can be directly computed. For example, the real-time-dependent cell-averaged current density can be obtained by taking the expectation value of the gauge invariant mechanical momentum:

$$\vec{J}(t) = -e \sum_{n,\bar{k}} \langle \psi_{n,\bar{k}}(t) | \hat{v} | \psi_{n,\bar{k}}(t) \rangle = -\frac{e}{m} \sum_{n,\bar{k}} \langle \psi_{n,\bar{k}}(t) | \hat{\pi} | \psi_{n,\bar{k}}(t) \rangle. \quad (2)$$

Here the gauge invariant mechanical momentum is defined as

$$\hat{\pi} = \frac{m}{i\hbar} [\hat{r}, \hat{H}] = \hat{p} + \frac{e}{c} \vec{A}(t) + \frac{im}{\hbar} [\hat{V}_{NL}, \hat{r}],$$

from which the velocity operator is given by $\hat{v} = \hat{\pi}/m$.

In this computation, the angular momentum dependent atomic potential is described by a separable form of a non-local pseudopotential (\hat{V}_{NL}), and thus the non-zero commutator with the position operator (\hat{r}) should be taken into account, as explained elsewhere [28]. Later for

the QSHI, our main interest will be focused on the spin current operator (\hat{j}^{S_z}) (see below) instead of the velocity operator ($\hat{\pi}/m$) used in Eq. (2).

If the parameters for the Hamiltonian, such as the E-field strength, are suitably chosen to make the adiabatic evolution, up to a first order variation of the wavefunctions, the velocity expectation can be written as [2],

$$\bar{v}_{n,\vec{k}}(t) = \frac{1}{m} \left\langle \psi_{n,\vec{k}}(t) \left| \hat{\pi}(t) \right| \psi_{n,\vec{k}}(t) \right\rangle = \frac{\partial \varepsilon_n(\vec{k}, t)}{\hbar \partial \vec{k}} - \frac{e}{\hbar} \vec{E} \times \Omega_n(\vec{k}, t), \quad (3)$$

where $\varepsilon_n(\vec{k}, t) = \left\langle \psi_{n,\vec{k}}(t) \left| \hat{H}_{KS}(t) \right| \psi_{n,\vec{k}}(t) \right\rangle$ is the instantaneous band energy, and $\Omega_n(\vec{k}, t) = \left\langle \partial u_{n,\vec{k}} / \partial \vec{k} \left| \times \right| \partial u_{n,\vec{k}} / \partial \vec{k} \right\rangle$ is the Berry curvature with $u_{n,\vec{k}}(\vec{r}, t)$ being the periodic part of the time-dependent KS wavefunctions $\psi_{n,\vec{k}}(\vec{r}, t) = e^{i\vec{r} \cdot \vec{k}} u_{n,\vec{k}}(\vec{r}, t)$. In the adiabatic regime, the wavefunction ($u_{n,\vec{k}}(\vec{r}, t)$), the band energy ($\varepsilon_n(\vec{k}, t)$), and the Berry curvature ($\Omega_n(\vec{k}, t)$) converge to the corresponding stationary values of the Bloch state with Bloch vector of $\vec{k} + e\vec{A}(t)$. To ensure that the time-propagating electron states adiabatically follow the ground state band structure, the E-field in the present calculations is smoothly turned on over a period of 10 to 25 fs, and the strength of the E-field ($|\vec{E}|$) is well below the Zener tunneling criterion [29]. Since the integral of the group velocity ($\partial \varepsilon_n(\vec{k}, t) / \partial \vec{k}$) over the BZ is zero, the integrated Berry curvature of the band can naturally be deduced from the integrated velocity:

$$\int_{BZ} \bar{v}_{n,\vec{k}}(t) d^2 \vec{k} = -\frac{e}{\hbar} \vec{E} \times \int_{BZ} \Omega_n(\vec{k}) d^2 \vec{k}.$$

Up to now, most first principles topological studies of real materials have employed the Wannierization method utilizing maximally localized Wannier functions (MLWFs) to compute the Berry curvature and to derive the topological numbers [13,15,30]. From the standpoint of the TKNN's equality, the topological nontrivial-ness of the insulators can be discussed in terms of physical quantity, such as charge or spin Hall conductivity [31,32]. However, such trials have mostly been hampered by the non-intuitiveness of spin Hall current, particularly, when the Hamiltonian is furnished with a measurable SOC of real materials [18,19,32]. Here, as the dynamical approach, noted in Eq.(1), provides a better computational versatility in dealing with experimentally accessible observables, we focus on the direct evaluation of the physical gauge-invariant velocity operator, as given in the left hand side of Eq. (3). This method requires only the occupied orbitals, and thus avoids the large sum over states of the response formula [14]. The required fine sampling of the BZ is here realized by the adiabatic sweep with a fine time step. Furthermore, even when an external field strongly perturbs the system, the expectation values, as given in the left hands side of Eq. (3), can naturally be evaluated, which can be utilized as a measure to capture the Berry curvature effects in non-adiabatic or non-equilibrium regime.

III. RESULTS AND DISCUSSION

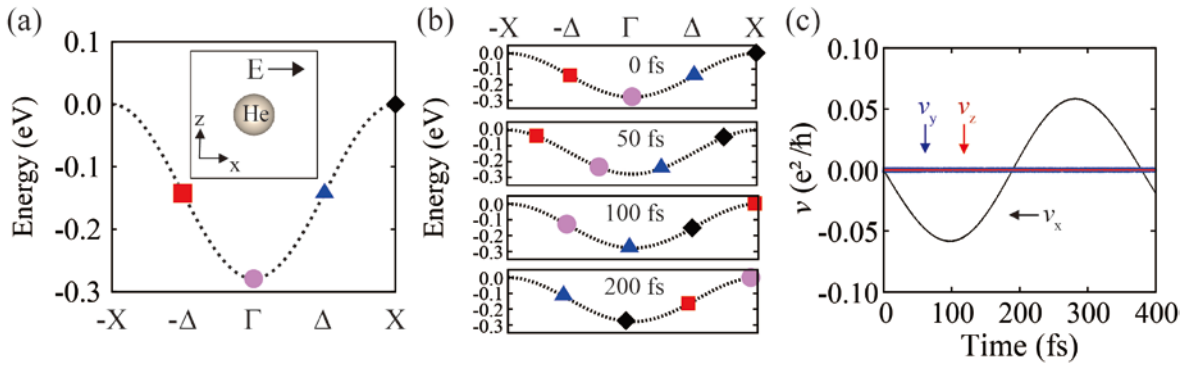


Figure 1. Time propagation of a KS band of a three-dimensional atomic insulator in response to an applied E-field. (a) The static band structure of the solid with He atom in a simple cubic cell. (b) Time variation of the band energy of four selected KS states. (c) Time variation of longitudinal (v_x) and transverse velocities (v_y and v_z) of the KS state starting from Γ point. Inset of (a) depicts the unit-cell with the indication of the E-field. In (a) and (b), the four selected Bloch states are denoted by the symbol of square, circle, triangle, and diamond.

A. Trivial atomic insulator

To demonstrate the efficiency in obtaining topological characteristics of materials from real-time evolving band states, we first consider the time evolution of a trivial insulator. As a representative example of an atomic insulator, here we devised a gedanken system by placing a He atom in the simple cubic (SC) lattice with a given fixed lattice constant of $a_0 = 3\text{\AA}$, as schematically depicted in inset of Fig. 1(a). The valence band is derived from the atomic $1s$ orbital, and the band dispersion is presented along the x-direction in Fig. 1(a). In this system, simultaneous presence of time-reversal and inversion symmetry enforces that $\Omega_n(\vec{k})=0$ at every \vec{k} point for the spin-frozen bands. Onto this self-consistently converged ground state, we applied a weak static electric field along the x-direction, $\vec{E} = 3.7 \times 10^{-3} \hat{x} \text{ V/\AA}$, and then the KS states are allowed to evolve over time. The selected KS states are depicted with symbols in Fig. 1(a) in unit of $b = 2\pi/a_0$: $\vec{k} = -\Delta(-0.25, 0, 0)$, $\Gamma(0, 0, 0)$, $\Delta(0.25, 0, 0)$, and $X(0.5, 0, 0)$. The time-evolving band energy of these KS states ($\varepsilon_{\vec{k}}(t) = \langle \psi_{\vec{k}}(t) | \hat{H}(t) | \psi_{\vec{k}}(t) \rangle$) is presented in Fig. 1(b) up to 200 fs. This model of an atomic insulator by construction possesses a large band gap

of $E_{gap} = 16.5$ eV, and the real-time evolutions of the KS states strictly follow the ground state energy surface. Figure 1(b) demonstrates that these evolving Bloch states ($\psi_{\vec{k}}(\vec{r}, t)$) move across the BZ along the ground state band with a time-evolving Bloch vector: $\psi_{\vec{k}_0}(\vec{r}, t) = \psi_{\vec{k}(t)}(\vec{r}, t = 0)$ given by $\vec{k}(t) = \vec{k}_0 - e\vec{E}t/\hbar$.

The time-profile of the velocity of the state starting from the Γ point (denoted by the circle in Fig. 1(a) and 1(b)) is shown in Fig. 1(c). It is noteworthy that the calculated transverse velocities always remain zero ($v_y(t) = v_z(t) = 0$), which is consistent with the absence of Berry curvature $\Omega(\vec{k}) = 0$ in this system. The other three sampled Bloch states also carry completely vanishing transversal velocities, as summarized in Appendix B. The calculated longitudinal velocity, using the formula given in the left hand side of Eq. (3), is indeed consistent with the instantaneous curvature of the band at \vec{k} : $v_x(t) = \left[\partial \varepsilon_{\vec{k}} / \hbar \partial k_x \right]_{\vec{k}=\vec{k}(t)}$. This periodic oscillation of the longitudinal velocity, with the period of $T = b_1 \hbar / eE_0 = 375$ fs as shown in Fig.1(c), originates from the periodic nature of the energy band in reciprocal cell, which can be compared to the Bloch oscillation [33].

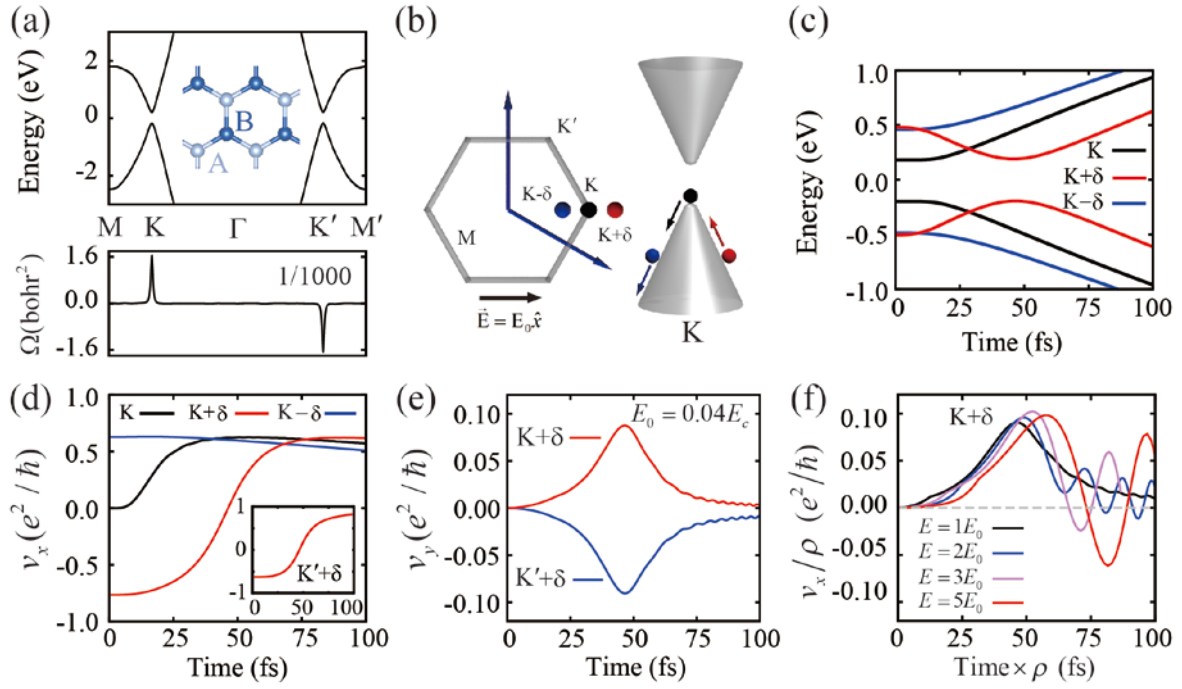


Figure 2. Time propagation of KS states in an inversion symmetry-broken graphene system. (a) The static band structure (upper panel) and the Berry curvature (lower panel) of the graphene whose inversion symmetry is broken by adding sublattice-asymmetric Hubbard U potential in the DFT+U. (b) Schematics of the BZ and the Dirac cone with three selected k-points in the K valley of the BZ. All three points are on the line along x-direction with $\delta = 0.03 \times 2\pi/a_0$, where $a_0 = 2.46 \text{ \AA}$ is the real-space lattice constant. (c) Time-variation of the band energies of the VBM and CBM states at the selected three k-points in the K valley. (d) Time profile of the longitudinal velocities of the states of the three k-points in the K valley. Inset shows the same longitudinal velocity of the point in the K' valley. (e) The time profile of the transverse velocity of the states starting from the K+ δ and K'+ δ points. (f) The same as (e) for the state starting from the K+ δ point with various strength of the E-field: $E = \rho E_0$. Here, E_0 indicates the strength of the E-field used for (c)(d)(e). The critical E-field in the Zener tunneling model (E_c)

is defined in the text. In the inset of (a), atomic symbols schematically depict the inversion-broken sub-lattices of two C atoms. All velocities in (d)(e)(f) are for the VBM state.

B. Valley Hall system: inversion symmetry-broken graphene

We now investigate a system which possesses a locally non-vanishing Berry curvature, but the band Chern number is absent owing to the presence of time-reversal symmetry. The simplest example in this perspective can be achieved from the spin-frozen bands of the graphene by intentionally breaking its inversion symmetry. To that end, we performed standard DFT+U calculation by adding an asymmetric U potential of $U = 4$ eV and 0 eV for A and B sites, respectively. As a result, the Dirac cones in the K and K' valleys develop a band gap of $E_{gap} = 0.39$ eV, as shown in the upper panel of Fig. 2(a). The Berry curvature of this artificially inversion-broken graphene bands are calculated and presented in the lower panel of Fig. 2(a) [9]. Onto the self-consistently converged ground state, we applied a constant and uniform static E-field along the x-direction ($\vec{E} = E_0 \hat{x} = 1.45 \times 10^{-3} \hat{x}$ V/Å) and performed the time propagation. The E-field was gradually turned on over initial 20 fs (see the Appendix A). The evolutions of three selected k-points near the K valley (K and $K \pm \delta$) are displayed in Fig. 2: the initial location of these three points is denoted in the BZ in Fig. 2(b), and the time profile of the band energies (the valence band maximum (VBM) and the conduction band minimum (CBM)) are summarized in Fig. 2(c). Note that, the state starting from the $K + \delta$ point (the red line Fig. 2(c)) arrives at the top of K valley at $t = 46.4$ fs. This time-evolution of band energies is schematically illustrated on the cone surface in Fig. 2(b).

The time-evolution of the longitudinal velocities $v_x(t)$ of these three selected VBM states in K valley is presented in Fig. 2(d). The calculated velocities coincide with the instantaneous slope of the band energy dispersion: for example, the state starting from the exact K point have zero initial velocity. It is noteworthy that, after around 70 fs, the velocities of all three states reveal a similar linear trend. After this time, all these three states move down the linear surface of the Dirac cone. We also performed the same calculation for the point in the K' valley, which showed the same longitudinal behavior as that in the K valley: the inset of Fig. 2(d) shows the velocity of the state starting from K'+ δ , which is almost identical to that starting from the K+ δ .

On the other hand, the transverse velocity of the states in the K valley are contrastingly different from those states in K' valley. Figure 2(e) shows that the transverse velocities of the state starting from K+ δ and K'+ δ points have opposite sign. This demonstrates that the spin-frozen bands of the inversion-broken graphene can indeed reveal the valley-Hall transport: the carriers in the K valley deflect with an opposite anomalous velocity from that in the K' valley [9]. In Fig. 2(c) and 2(d), we demonstrate that the two states arrive at the top of the valley at around 46 fs, leading to zero-longitudinal velocity. At this point the instantaneous velocities consist only of the anomalous velocity given by $v_y(t) = \frac{e}{\hbar} E_0 \Omega$, which directly monitors the Berry curvature on the peak point [9]. The Berry curvature obtained by this way is $\Omega_{K,K'} = \hbar v_y / e E_0 = \pm 1599 \text{ bohr}^2$, which is comparable to the value of $\Omega_{K,K'} = \pm 1646 \text{ bohr}^2$ obtained from the Kubo formula with Wannierized bands (See the lower panel of Fig. 2(a)) [14].

This example thus suggests that the real-time propagation of the KS equations can indeed be employed to evaluate the Berry curvature, Hall conductivity, and consequently the band Chern number, by choosing a reasonable parameter, such as a modestly weak E-field. To make the time-evolving states follow well the adiabatic energy surfaces, the strength of E-field needs to be sufficiently weak compared to the band gap (E_{gap}). This feature can be discussed quantitatively in terms of Zener tunneling model [29]: the critical strength of an E-field to induce tunneling across the band gap is estimated to be $E_c = \frac{\pi}{2\hbar} \sqrt{m_r E_{gap}^3}$, where m_r is the reduced effective mass between the CBM and the VBM. The E-field used for Fig. 2(c)(d)(e) ($E_0 = 1.45 \times 10^{-3} \text{ V/\AA}$) corresponds to $E_0 = 0.04 E_c$. In Fig. 2(f), we compare the simulation results with four different strengths of the E-field: $E = \rho E_0$ with $\rho = 1, 2, 3, 5$. It is noteworthy that, for $E \geq 0.08 E_c$, an abrupt oscillatory feature emerges as the Bloch state passes the Dirac cone region, which indicates the hybridization of CBM and VBM states, and consequently a breakdown of the adiabaticity.

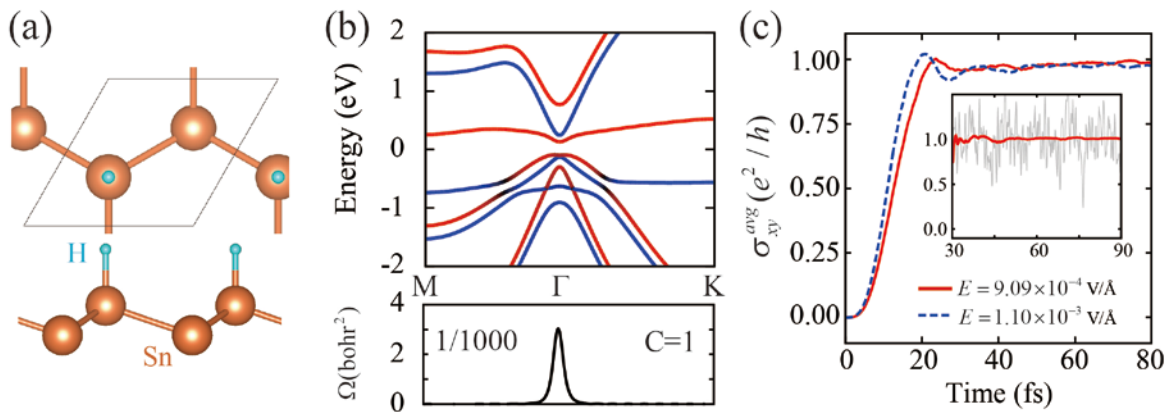


Figure 3. Time propagation of the KS states of the ideal half-hydrogenated Sn in a quantum anomalous Hall phase. (a) Schematic geometry, (b) the band structure and Berry curvature, and

(c) the time-averaged Hall conductivity calculated from the time-evolving states. Red and blue colors in lines in (b) represent the texture of the spin polarization in positive and negative z -direction, respectively. The inset of (c) shows the real-time profile (gray) and the time-averaged profile (red) of the Hall conductivity after the turning-on period.

C. Quantum anomalous Hall insulator

Our method of time-propagation can also be directly applied to the QAH case. Since the first experimental realization of the QAH phase on a magnetized topological insulator [16], various studies ensued to find a new material that can preserve the intrinsic quantum Hall conductivity in an elevated temperature. Several works, in this perspective, have focused on the possible transitions of a 2D hexagonal lattice from the QSH to the QAH [23,34]. One of the most intriguing examples in this direction is the single layer of Sn [35], named stanene, with various hydrogen or halogens coverages: the full coverage of halogens reveals a QSH phase, whose band structures can be described with the Bernevig-Hughes-Zhang (BHZ) model Hamiltonian, while the ideal half coverage on one side results in QAH phase [34]. Hereafter, this half-hydrogenated Sn, as depicted in Fig. 3(a), is abbreviated as HHS. Prior to the evaluation of the time-evolving state, we calculated the static ground state band structure, and also the Berry curvature using MLWFs, as summarized in Fig. 3(b). In agreement with the previous study, HHS exhibits a highly localized peak in the Berry curvature ($\Omega_{\Gamma} = 3026 \text{ bohr}^2$) around the Γ point, which is integrated to a single quantum of the Chern number ($C = 1$) [34].

To evaluate the charge Hall conductivity from the expectation value of the velocity operator, as noted in Eq.(2) and Eq.(3), we applied a static E-field in the x -direction and

performed the time propagation of the uniformly sampled Bloch states. Since the band gap in this case is quite small, to achieve a reasonable adiabatic quality, we chose smaller strengths of the E-field which was turned-on gradually over 25 fs period. The transverse current is calculated from the time-evolving Bloch states, and the Hall conductivity is given by

$$\sigma_{xy}(t) = \frac{J_y}{E_x} = -\frac{1}{mE_x} \sum_{n,\bar{k}} \langle \psi_{n,\bar{k}}(t) | \hat{\pi}_y | \psi_{n,\bar{k}}(t) \rangle. \quad (4)$$

The calculation results are presented in Fig. 3(c), which shows that, after the initial turning-on period ($t_0 = 25$ fs), the time-averaged profile $\sigma_{xy}^{avg}(t) = \frac{1}{t-t_0} \int_{t_0}^t \sigma_{xy}(\tau) d\tau$ converges well to the single quantum of the conductance. In this QAH phase of HHS, the Berry curvature is not dominated by a single band, but rather distributed over multiple bands around the Γ point [34], where the inverted VBM and CBM states are intricately hybridized. However, the Hall current calculated as a sum of occupied valence bands reveals a good convergence. Detailed electronic band structures for HHS is given in the Appendix C.

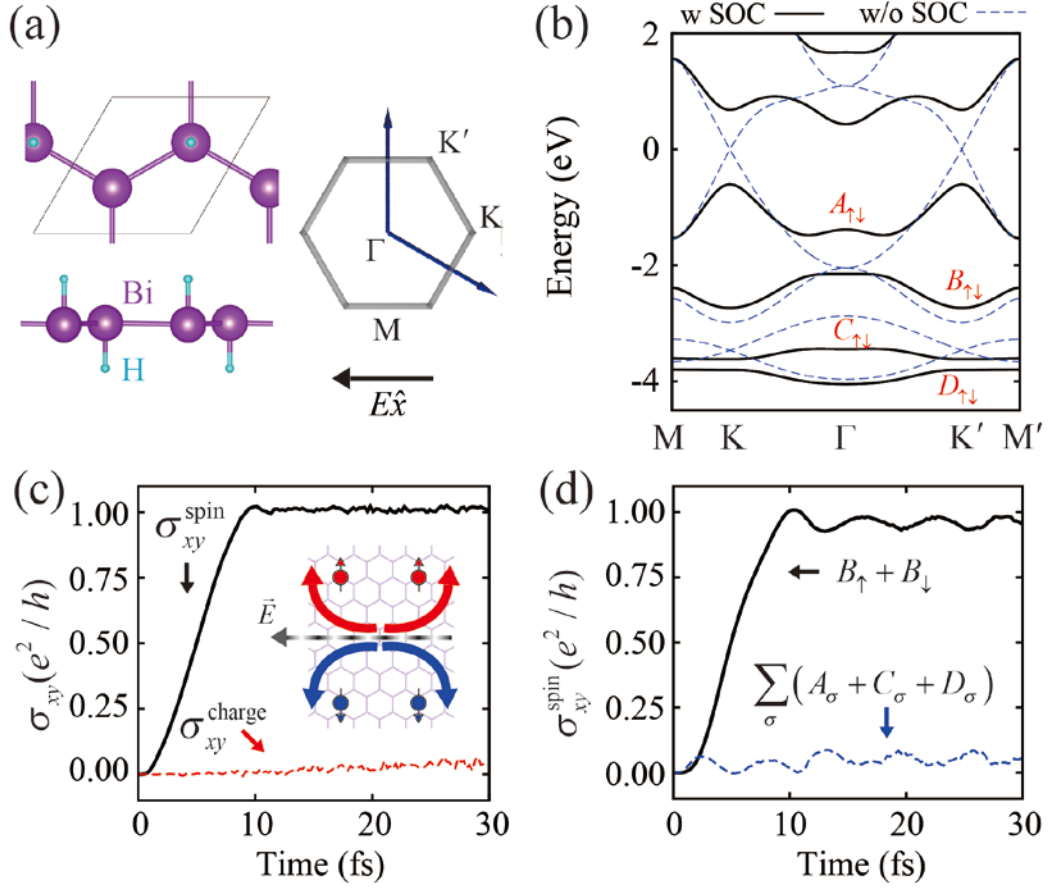


Figure 4. Time propagation of the KS states of the bismuthane in a quantum spin Hall phase. (a) Schematics of the geometry and the BZ. (b) Band structures with (solid line) or without (dashed line) SOC. Doubly degenerate valence bands are labeled A to D from the highest band. (c) The spin Hall conductivity and the charge Hall conductivity calculated from the time-evolving states. (d) The band-resolved contributions to the spin Hall conductivity from the doubly degenerate second valence band (B) and from the rest (A+C+D). Inset of (c) depicts the bias static E-field and the spin-resolved current.

D. Quantum spin Hall insulator

We now extend our example of the time-evolution study to a QSHI. As an example, we

calculated the single layer bismuthane in which the hydrogenated Bi atom locates in the hexagonal lattice [23,36], as shown in Fig. 4(a). When the spin-orbit coupling (SOC) is intentionally turned off, the band structure reveals the typical Dirac cone structure of a honeycomb bipartite lattice, as depicted by the dashed line in Fig. 4(b). When we include the SOC of Bi atoms, the bands near the Dirac cones open a gap of 0.8 eV at K and K' points, as presented with solid lines. The optimized geometry of the layer has small buckling but preserves the inversion symmetry, and thus the spinor states in the K and the K' valley constitute the time-reversal and inversion partners, enforcing the spin-up and spin-down states to be degenerated over the whole BZ [18,23]. Results for a similar system without inversion symmetry is presented in the Appendix D. In Fig. 4(b), the valence bands are labelled from A to D, where the up and down arrows in the subscript (*e.g.* $A_{\uparrow\downarrow}$) indicates the doubly degenerate bands. It should be noted that the spin in this case is not well polarized in the z-direction, but has varying textures depending on the k-points as a result of the strong SOC.

We computed the electron dynamics of this QSHI system, by gradually ramping the E-field over 10 fs towards a static value of $\vec{E} = 3.37 \times 10^{-6} \hat{x}$ V/Å. As we above enumerated the charge current as an expectation value from the time-evolving wavefunctions, the spin value and the spin current can also be computed as an expectation value from these spinor wavefunctions. There has been quite a lot of theoretical works to devise a better form of the spin current operator [10,37-39]. Here we choose the operator in the following form, as represented in the Heisenberg picture,

$$\hat{j}^{s_z} = e \frac{d}{dt} (\hat{r} \hat{S}_z) = \frac{e}{2m} \{ \hat{\pi}, \hat{S}_z \} + \hat{r} \frac{e}{i\hbar} [\hat{S}_z, \hat{H}]. \quad (5)$$

In our actual computation results, the effect of second term in Eq. (5) was found to be two orders of magnitude smaller than the first term, thus for this system the very classical form of the spin current operator (the first term of Eq. (5)) works efficiently. The second term, though not present explicitly in the following discussions, was fully accounted for in numerical calculations. Note that, since the total spin of the unit-cell is consistently zero, the second term is well defined even for the periodic solid without gauge ambiguity. The spin-Hall conductivity of the z-polarized spin, as defined below in Eq. (6), and the charge-Hall conductivity, as defined in Eq. (4), are presented in Fig. 4(c).

$$\sigma_{xy}^{\text{spin}}(t) = -\frac{1}{E_x} \sum_{n,\bar{k}} \langle \psi_{n,\bar{k}}(t) | \hat{J}_y^{S_z} | \psi_{n,\bar{k}}(t) \rangle = -\frac{1}{2mE_x} \sum_{n,\bar{k}} \langle \psi_{n,\bar{k}}(t) | \{ \hat{S}_z, \hat{\pi}_y \} | \psi_{n,\bar{k}}(t) \rangle. \quad (6)$$

Remarkably, even though S_z is not a good quantum number and varies over different k-points [38], the spin-Hall conductivity converges well to the conductivity quantum just after the initial turning-on period of the E-field. On the other hand, the charge-Hall conductivity consistently remained to zero, which is a natural outcome of the time-reversal symmetry of the system. As depicted in the inset of Fig. 4(c), the longitudinal current of the insulator is summed to zero, but the Hall current of each spin sector was directed oppositely, as a result, producing a finite spin-Hall current.

The band-resolved contribution of each doubly degenerate valence bands (denoted by A , B , C , and D in Fig. 4(b)) to the spin-Hall conductivity is presented in Fig. 4(d). We observe that the QSH phase of bismuthane is dominated solely by the second valence bands (B), while the effects of the rest (A , C , D) are marginal. This can be explained by the structure of the band inversions, which can be inferred from the comparison between the bands with and without SOC. The band C and D are inverted at K and K' ; and the VBM band (A) has two points of

band inversion: one with the CBM band at K and K' , and the other with the band B at Γ . This double inversion renders the band A topologically trivial, and the full occupation of the inverted pair of C and D bands makes their topology (the spin Chern number) cancel each other. As a result, the band B , which is doubly degenerate and is solely inverted from the band A at Γ , remains as a single source of the quantized spin Hall state.

Here, we need to discuss more in-depth the structure of the Berry curvature of the QSHI state. The degeneracy in the valence bands requires the Berry curvature to be defined as a matrix constructed in the degenerate subspace, putting in evidence its the non-Abelian character [2,39]. The components of the Berry curvature matrix (Ω), and of the spin matrix (S_z), depend on the choice of the basis (gauge-dependent), and thus cannot be observed in an experiment. Physical observables are gauge-independent, and it is shown that the charge Hall and the spin Hall current can be written in terms of $\text{Tr}[\Omega]$ and $\text{Tr}[S_z\Omega]$, respectively [39]. In this regard, our approach through the expectation value of the physical observables (charge or spin current operator, as given in Eq. (4) and Eq. (6)) is advantageous over other methods: the spin Hall current, as presented in Fig. 4(c), do not require any additional cost or separate treatment due to the degeneracy. Moreover, since the expectation value of an operator is independent of the unitary rotation within the degenerate subspace, the spin current can be written in terms of the velocity given by the diagonalized basis at each k -point:

$$\begin{aligned} \frac{1}{2} \sum_{n,\bar{k}} \langle \psi_{n,\bar{k}}(t) | \{ \hat{S}_z, \hat{\pi}_y \} | \psi_{n,\bar{k}}(t) \rangle &= \frac{1}{2} \sum_{\bar{k}} \sum_n \langle \psi_{n,\bar{k}}(t) | \hat{U}_{\bar{k}}^\dagger \{ \hat{S}_z, \hat{\pi}_y \} \hat{U}_{\bar{k}} | \psi_{n,\bar{k}}(t) \rangle \\ &= \sum_{\bar{k}} \frac{\hbar}{2} \langle \psi_{\uparrow,\bar{k}}(t) | \hat{\pi}_y | \psi_{\uparrow,\bar{k}}(t) \rangle - \sum_{\bar{k}} \frac{\hbar}{2} \langle \psi_{\downarrow,\bar{k}}(t) | \hat{\pi}_y | \psi_{\downarrow,\bar{k}}(t) \rangle \end{aligned} \quad (7)$$

The form of the last expression of Eq. (7) is valid regardless of whether the spin is well defined

as a good quantum number throughout the whole BZ or varies over k-points. This suggests that the spin-Hall conductivity, as written Eq. (6), can be used to identify the spin Chern number, exactly in the same way as introduced in the simplified Kane-Mele model [18,19], even when a strong SOC demotes the spin from the status of good quantum number of the system [20,32]. In the Appendix D, we present the same results for an inversion symmetry-broken bismuthane, in which the degeneracy is modestly lifted, but the calculated spin-Hall conductivity converges well into the quantized value, identifying its QSH phase.

IV. CONCLUSIONS AND OUTLOOK

In summary, we demonstrated here that the real-time propagation of the Kohn-Sham Bloch states, and the corresponding time-dependent current obtained, provides a completely alternative method to explore the topological character of solids. Results for exemplary cases were presented; including a trivial atomic insulator, a valley Hall system, and a quantum anomalous Hall system. On a prototypical example of the quantum spin Hall insulator, we discussed that this direct evaluation of the physical observables can serve as a natural platform for an adequate description of the non-Abelian Berry curvature. The concept suggested here is not necessarily limited to the DFT-based mean-field scheme. One-body physical observables (such as charge or spin current), derivable from the time-evolving many-body states, can be employed to gauge the anomalous behaviors rooted in the geometrical phase structures of the quantum mechanical wavefunctions.

As an outlook we outline that the flexibility of the proposed computation scheme provides an additional important advantage: general time-dependent perturbations that can be included in the vector potential (see Eq.(1)) enables the simulation of non-adiabatic or non-equilibrium

situations. Recently, many studies have focused on the effect of external forces which dynamically perturb the time-reversal symmetry of the system [40-47]. For such driven systems, a time-dependent current can be better experimentally accessible than the topological numbers defined in the frequency domain [7,48-53]. To illustrate the new possibility offered by our approach, we calculated the current flow along a graphene nano-ribbon and show that the system develops a Hall voltage when a circularly polarized driving force is applied, as a source of externally driven time-reversal breaking mechanism (see appendix E). The present work provides the theoretical framework to unambiguously address topological features of driven matter that can be linked to experimental observables.

VI. ACKNOWLEDGEMENTS

We acknowledge financial support from the European Research Council (ERC-2015-AdG-694097) and Grupos Consolidados UPV/EHU (IT578-13). The Flatiron Institute is a division of the Simons Foundation. SAS gratefully acknowledges the support from Alexander von Humboldt Foundation. DS and NP acknowledge the support from NRF through the Basic Research Laboratory (NRF-2017R1A4A1015323) and the Basic Science Research Program (NRF-2016R1D1A1B03931542).

APPENDIX A : Parameters for the ground state DFT and time-integration algorithms

The equilibrium atomic geometry and the ground state electronic structure are obtained by

standard density functional theory (DFT) calculation using Octopus and Quantum Espresso package [26,27,54-56]. To describe the exchange and correlation of electrons, Perdew-Burke-Ernzerhof (PBE)-type generalized gradient approximation functional is employed [57]. The nuclei potentials are described by norm-conserving pseudopotentials. The Brillouin zone is integrated using Monkhorst-Pack scheme: the grid of $6 \times 6 \times 6$, $12 \times 12 \times 1$, $20 \times 20 \times 1$, and $9 \times 9 \times 1$ is used for the solid He, Graphene, half-passivated Stanene, and Bismuthane, respectively. To optimize the geometry, the forces on each atom are relaxed within 10^{-5} Ry/Bohr. To propagate the KS states, we start with the ground state orbitals at $t = 0$, obtained by standard DFT calculation. The wavefunction at $t + \Delta t$ is evolved from that at t with

$$\psi_n(t + \Delta t) = \exp\left(-i\Delta t \hat{H}[\rho(t)]/\hbar\right)\psi_n(t). \quad (\text{A1})$$

For the time-dependent Hamiltonian, the external time-dependent potential is added to the Kohn-Sham Hamiltonian constructed as a functional of the density at time t . In Eq. (A1), the band index and the Bloch vector are collectively denoted by the subscript n . The evolved charge density $\rho(t + \Delta t)$ is calculated from the squared sum of the evolved KS wavefunctions:

$$\rho(t + \Delta t) = \sum_n |\psi_n(t + \Delta t)|^2, \quad \text{from which the KS Hamiltonian at the next time step}$$

$H[\rho(t + \Delta t)]$ is again derived. A few algorithms have been tested in the literature to achieve a better consistency between wavefunctions and the Hamiltonian. For example, the consistency of the density at the intermediate step between that of forward evolution from the previous step and that of backward evolution from the next step is a good criterion. Many detailed formalisms regarding this method were published by numerous authors including us [25,26,58,59].

Static constant uniform electric field (E-field) is expressed in the velocity gauge as a

vector potential through the relation: $\vec{E} = \frac{1}{c} \partial \vec{A}(t) / \partial t$. However, throughout our works, to achieve a better adiabatic evolution, the E-field is gradually turned-on during the initial period (τ):

$$A(t) = \begin{cases} cE_0 (t^3 / \tau^2 - 0.5t^4 / \tau^3), & 0 \leq t < \tau \\ cE_0 (t - 0.5\tau), & t \geq \tau \end{cases}. \quad (\text{A2})$$

Note that after the turn-on period ($t \geq \tau$) the E-field strength becomes constant over time (E_0).

In the present work, we mainly aimed at materials intrinsic topological property and thus focused on the weak-field regime. In this context, the vector potential is provided purely externally, and the back reaction of the material into the field is not considered. When the material's feedback is substantial, the response of the vector field needs to be considered as suggested by Bertsch et al. [60].

APPENDIX B: Time profiles of KS states of the artificial He simple cubic solid

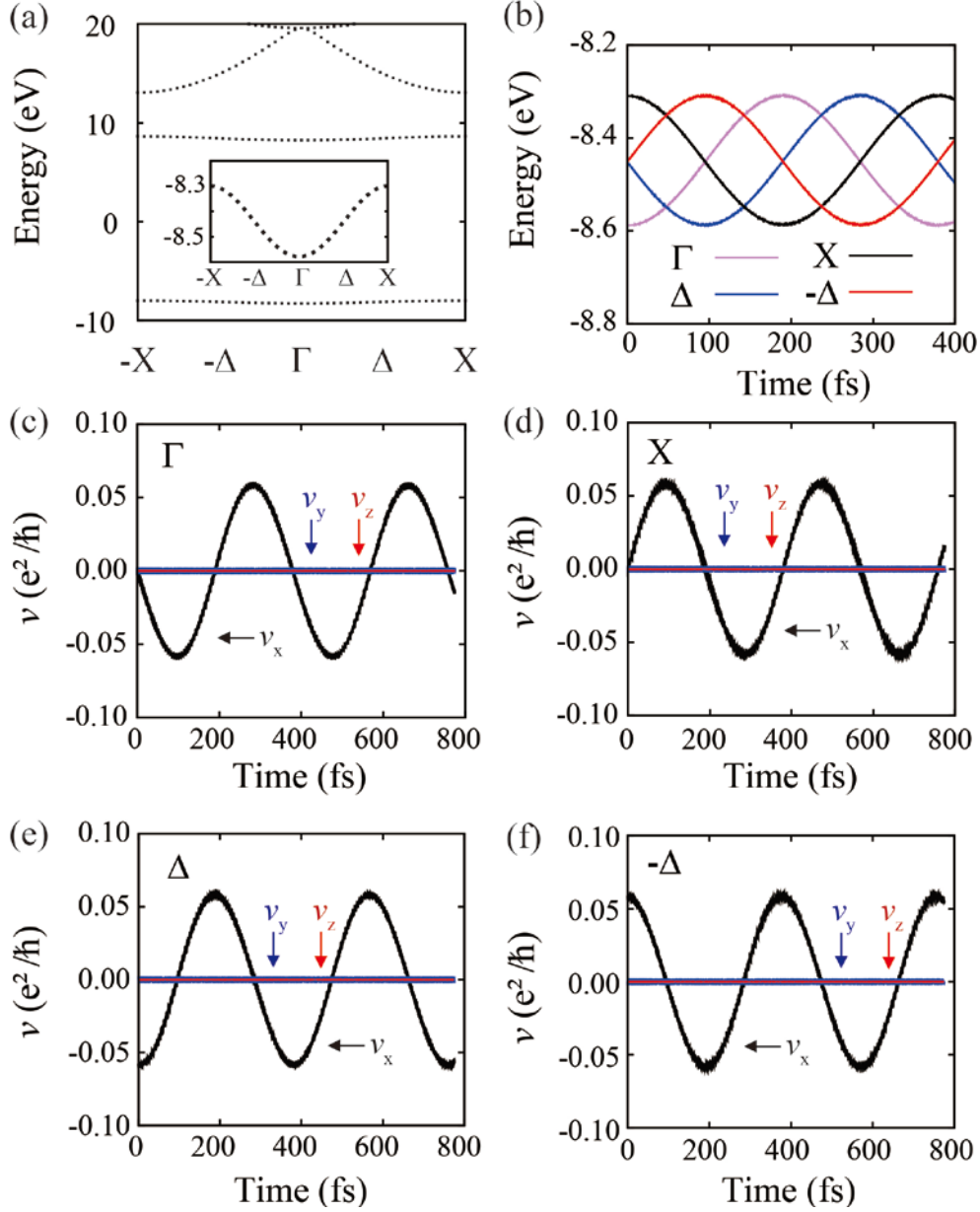


Figure 5. Time evolution of KS states in artificial solid He. (a) Band structure of solid He system in the simple cubic lattice of 3\AA lattice constant. (b) Time-variation of the band energy of the four selected states. The velocity of the Bloch state departed from (c) Γ , (d) X , (e) Δ , and (f) $-\Delta$. Inset in (a) is the valence band presented in the narrower energy window, exactly the same as in Fig. 1(a)

Here we show a detailed time profile of the four selected states in the valence band of He solid, which was introduced in Fig. 1 of the main text: Γ , X, Δ , and $-\Delta$. As shown in Fig. 1(a) and Fig. 5(a), the band gap is so wide (16.5 eV), and the time profiles of the KS states follow the static energy band very closely: Figure 1(b) and Fig. 5(b) tells that the instantaneous band energy is $\varepsilon(t) = \varepsilon(\vec{k}(t))$ with $\vec{k}(t) = \vec{k}(0) - et\vec{E}/\hbar$. The velocity given by the band energy dispersion, $v(\vec{k}) = \frac{1}{\hbar} \frac{d\varepsilon(\vec{k})}{d\vec{k}}$, is presented in Fig. 5(c)-(f) for each of the state starting from Γ , X, Δ , and $-\Delta$. Note that, with the given E-field strength, these velocities well produces the oscillation period of $T=375\text{fs}$, which corresponds to the time required for the Bloch state to travel the whole BZ : $(eE/\hbar)T = 2\pi/a_0$.

APPENDIX C: The electronic structure of the half-hydrogenated Sn

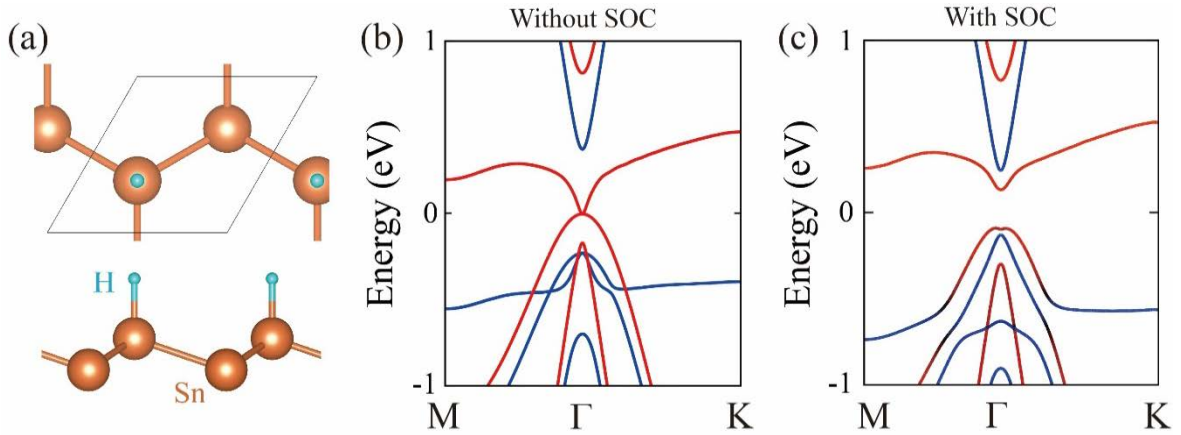


Figure 6. Band structure of stanene with hydrogen half passivation. (a) schematic geometry and band structure of stanene with the half coverage of hydrogen passivation (b) with and (c) without spin orbit coupling. Red and blue indicate spin-up and spin-down states which are polarized along the out-plane direction.

The electronic structure of stanene with the half coverage of the hydrogen passivation, abbreviated as HHS in the main text, is presented in Fig. 6(a), which is qualitatively the same as the previously reported passivation with halogen atoms [34]. Figure 6(b) shows that, when SOC is not counted, the spin-down bands (blue) reveals a gap, while the spin-up bands (red) produce metallic states. Upon the inclusion of realistic SOC, the spin-up bands near the Fermi level are inverted, as presented in Fig. 6(c).

APPENDIX D: QSH phase of half-hydrogen passivated bismuthane

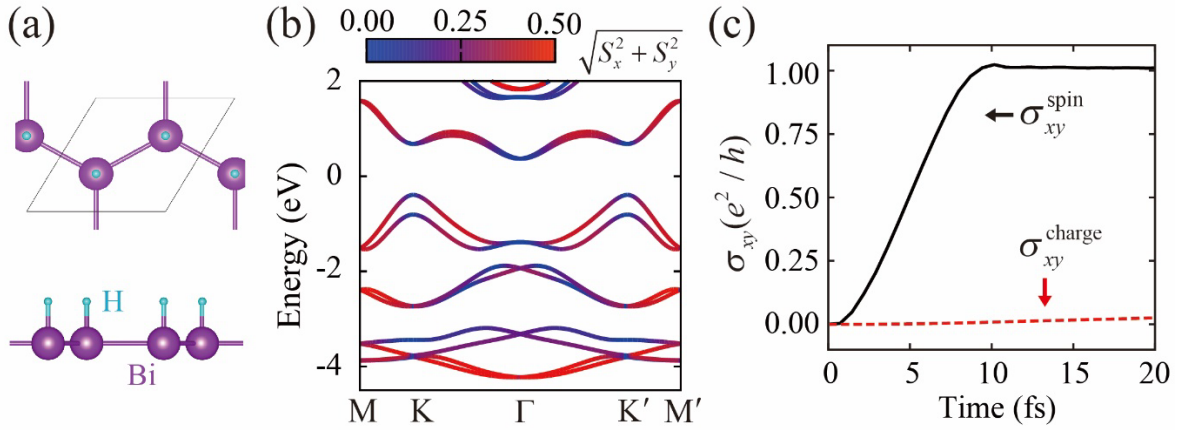


Figure 7. QSH phase of the inversion symmetry broken Bismuthane. (a) Schematic geometry with the hydrogen coverage on one side. (b) The spin resolved band structure. (c) Spin and charge Hall conductivity calculated by TDDFT. In (b), the color depicts the magnitude of the in-plane component of the spin.

As an additional example of a QSHI, here we consider the inversion symmetry broken

bismuthane. When hydrogen atoms are attached only onto the single side of the bismuthine, as shown in Figure 7(a), the spinor bands are split and the spin textures are almost lying in the plane, as shown in Figure 7(b). The expectation of the spin current operator and charge current operator are calculated with the time-evolving Kohn-Sham spinor states. The obtained spin Hall and charge Hall conductivity, as defined in Eq. (4). And Eq. (6) in the main text, are summarized in Fig. 7(c).

APPENDIX E: Effect of a circularly polarized external field on a zig-zag graphene nano-ribbon

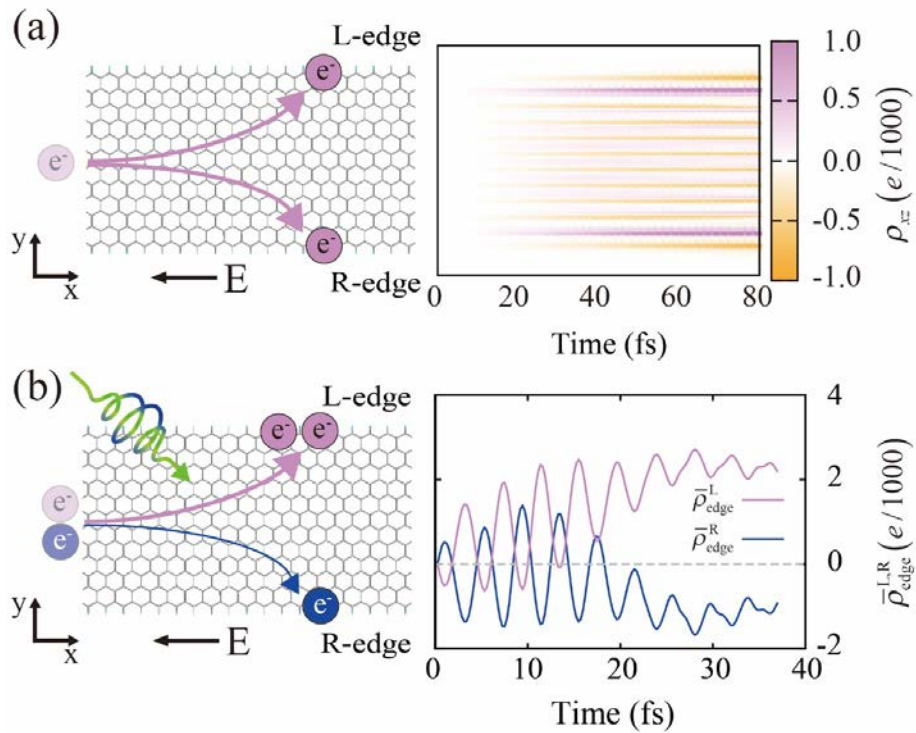


Figure 8. Current flow in a graphene nano-ribbon biased by a static E-field. (a) Schematic of valley Hall effect (left) and the calculation results for the time-varying charge density. (b) The same as (a) but with a circularly polarized E-field in addition to the static axial bias. In (a) and

(b), the time-varying charge density is obtained by $\rho_{xz}(y, t) = \iint dx dz [\rho(\vec{r}, t) - \rho_0(\vec{r})]$, and

$\bar{\rho}_{\text{edge}}^L$ and $\bar{\rho}_{\text{edge}}^R$ are the time-averaged charge obtained in each edge region of the ribbon

$$(W=26\text{\AA}): \bar{\rho}_{\text{edge}}^L(t) = \frac{1}{t} \int_0^t d\tau \int_{0.8W}^{\infty} \rho_{xz}(y, \tau) dy \quad \text{and} \quad \bar{\rho}_{\text{edge}}^R(t) = \frac{1}{t} \int_0^t d\tau \int_{-\infty}^{0.2W} \rho_{xz}(y, \tau) dy$$

To illustrate how our calculation method of physical observable through the TDDFT can include the effect of external time-dependent field, here we calculate the current through a graphene nano-ribbon (GNR) with and without applying a circularly polarized external E-field.

Figure 8(a) depicts the real-time variation of electron density when a constant static bias ($\vec{E} = 1.68 \times 10^{-3} \hat{x} \text{ V/\AA}$) is applied along the ribbon axial direction. As described in main text, we calculate the time-evolving Kohn-Sham states, and the time-varying density is obtained from the squared sum of the wavefunctions. As the time evolves, the charge accumulates on both edges, depleting the central region of the ribbon, which can be attributed to the valley-Hall nature of the ribbon [9]. However, since the system preserves the overall time-reversal symmetry, the ribbon does not develop any transversal charge, and thus any Hall voltage. When a time-dependent external field is added, in particular when it is circularly polarized, the situation can be remarkably changed: in Figure 8(b), the Kohn-Sham wavefunctions and the charge densities are calculated with the circularly polarized E-field of $\vec{E} = 6.7 \times 10^{-4} (\hat{x} + i\hat{y}) e^{-i\omega t} \text{ V/\AA}$, with $\omega = 1 \text{ eV}$, in addition to the static bias. Remarkably, the two edges (L and R) now lose the symmetry, and the system develops an overall charge Hall effect across the ribbon width [40]. This can be conceived as a real-time manifestation of an effective time-reversal breaking by a circularly polarized external field.

Numerous studies have discussed the topological natures of driven states, particularly focusing onto the time-reversal broken features effected by a circularly polarized field [40-47]. Our method, that calculates the physical observables from time-evolving Kohn-Sham states under such external fields provide results directly accessibly in experiments.

VII. REFERENCES

- [1] M. V. Berry, Proc. R. Soc. Lon. Ser-A **392**, 45 (1984).
- [2] D. Xiao, M. C. Chang, and Q. Niu, Rev. Mod. Phys. **82**, 1959 (2010).
- [3] D. J. Thouless, M. Kohmoto, M. P. Nightingale, and M. denNijs, Phys. Rev. Lett. **49**, 405 (1982).
- [4] S. S. Chern and J. Simons, Ann. Math. **99**, 48 (1974).
- [5] A. Bansil, H. Lin, and T. Das, Rev. Mod. Phys. **88**, 021004 (2016).
- [6] D. N. Basov, R. D. Averitt, and D. Hsieh, Nat. Mater. **16**, 1077 (2017).
- [7] Y. Tokura, M. Kawasaki, and N. Nagaosa, Nat. Phys. **13**, 1056 (2017).
- [8] J. Sinova, S. O. Valenzuela, J. Wunderlich, C. H. Back, and T. Jungwirth, Rev. Mod. Phys. **87**, 1213 (2015).
- [9] D. Xiao, W. Yao, and Q. Niu, Phys. Rev. Lett. **99**, 236809 (2007).
- [10] J. Sinova, D. Culcer, Q. Niu, N. A. Sinitsyn, T. Jungwirth, and A. H. MacDonald, Phys. Rev. Lett. **92**, 126603 (2004).
- [11] K. F. Mak, K. L. McGill, J. Park, and P. L. McEuen, Science **344**, 1489 (2014).
- [12] D. Go, D. Jo, C. Kim, and H. W. Lee, Phys. Rev. Lett. **121**, 086602 (2018).
- [13] N. Marzari, A. A. Mostofi, J. R. Yates, I. Souza, and D. Vanderbilt, Rev. Mod. Phys. **84**, 1419 (2012).
- [14] X. J. Wang, J. R. Yates, I. Souza, and D. Vanderbilt, Phys. Rev. B **74**, 195118 (2006).
- [15] D. Gosalbez-Martinez, I. Souza, and D. Vanderbilt, Phys. Rev. B **92**, 085138 (2015).
- [16] C. Z. Chang *et al.*, Science **340**, 167 (2013).
- [17] F. D. M. Haldane, Phys. Rev. Lett. **61**, 2015 (1988).
- [18] C. L. Kane and E. J. Mele, Phys. Rev. Lett. **95**, 226801 (2005).
- [19] C. L. Kane and E. J. Mele, Phys. Rev. Lett. **95**, 146802 (2005).
- [20] B. A. Bernevig, T. L. Hughes, and S. C. Zhang, Science **314**, 1757 (2006).
- [21] M. König, S. Wiedmann, C. Brune, A. Roth, H. Buhmann, L. W. Molenkamp, X. L. Qi, and S. C. Zhang, Science **318**, 766 (2007).
- [22] Y. Xu, B. H. Yan, H. J. Zhang, J. Wang, G. Xu, P. Z. Tang, W. H. Duan, and S. C. Zhang, Phys. Rev. Lett. **111**, 136804 (2013).
- [23] K. H. Jin and S. H. Jhi, Sci. Rep. **5**, 8426 (2015).
- [24] M. Z. Hasan and C. L. Kane, Rev. Mod. Phys. **82**, 3045 (2010).
- [25] D. Shin, G. Lee, Y. Miyamoto, and N. Park, J. Chem. Theory Comput. **12**, 201 (2016).
- [26] A. Castro, M. A. L. Marques, and A. Rubio, J. Chem. Phys. **121**, 3425 (2004).
- [27] P. Giannozzi *et al.*, J. Phys-Condens. Mat. **21**, 395502 (2009).
- [28] C. D. Pemmaraju, F. D. Vila, J. J. Kas, S. A. Sato, J. J. Rehr, K. Yabana, and D. Prendergast, Comput. Phys. Commun. **226**, 30 (2018).
- [29] E. O. Kane, J. Phys. Chem. Solids **12**, 181 (1959).
- [30] A. A. Soluyanov and D. Vanderbilt, Phys. Rev. B **83**, 035108 (2011).
- [31] B. A. Bernevig and S. C. Zhang, Phys. Rev. Lett. **96**, 106802 (2006).
- [32] O. F. Dayi and E. Yunt, Int. J. Geom. Methods M. **13**, 1550136 (2016).
- [33] M. BenDahan, E. Peik, J. Reichel, Y. Castin, and C. Salomon, Phys. Rev. Lett. **76**, 4508 (1996).
- [34] S. C. Wu, G. C. Shan, and B. H. Yan, Phys. Rev. Lett. **113**, 256401 (2014).
- [35] F. F. Zhu, W. J. Chen, Y. Xu, C. L. Gao, D. D. Guan, C. H. Liu, D. Qian, S. C. Zhang, and J. F. Jia, Nat. Mater. **14**, 1020 (2015).
- [36] F. Reis, G. Li, L. Dudy, M. Bauernfeind, S. Glass, W. Hanke, R. Thomale, J. Schafer, and R. Claessen, Science **357**, 287 (2017).
- [37] J. R. Shi, P. Zhang, D. Xiao, and Q. Niu, Phys. Rev. Lett. **96**, 076604 (2006).
- [38] S. Murakami, Phys. Rev. Lett. **97**, 236805 (2006).
- [39] M. Gradhand, D. V. Fedorov, F. Pientka, P. Zahn, I. Mertig, and B. L. Gyorffy, J. Phys-Condens. Mat. **24**, 213202 (2012).
- [40] T. Oka and H. Aoki, Phys. Rev. B **79**, 081406(R) (2009).
- [41] E. J. Sie, J. McIver, Y. H. Lee, L. Fu, J. Kong, and N. Gedik, Nat. Mater. **14**, 290 (2015).
- [42] M. Claassen, C. J. Jia, B. Moritz, and T. P. Devereaux, Nat. Commun. **7**, 13074 (2016).
- [43] M. A. Sentef, M. Claassen, A. F. Kemper, B. Moritz, T. Oka, J. K. Freericks, and T. P. Devereaux, Nat. Commun. **6**, 7047 (2015).
- [44] S. Y. Yao, Z. B. Yan, and Z. Wang, Phys. Rev. B **96**, 195303 (2017).
- [45] Q. Chen, L. Du, and G. A. Fiete, Phys. Rev. B **97**, 035422 (2018).

- [46] H. Hübener, M. A. Sentef, U. De Giovannini, A. F. Kemper, and A. Rubio, *Nat. Commun.* **8**, 13940 (2017).
- [47] D. Shin, H. Hübener, U. De Giovannini, H. Jin, A. Rubio, and N. Park, *Nat. Commun.* **9**, 638 (2018).
- [48] Z. F. Wang, Z. Liu, J. L. Yang, and F. Liu, *Phys. Rev. Lett.* **120**, 156406 (2018).
- [49] T. Mikami, S. Kitamura, K. Yasuda, N. Tsuji, T. Oka, and H. Aoki, *Phys. Rev. B* **93**, 144307 (2016).
- [50] M. Sato, S. Takayoshi, and T. Oka, *Phys. Rev. Lett.* **117**, 147202 (2016).
- [51] T. Oka and S. Kitamura, arXiv:1804.03212v1 (2018).
- [52] I. Esin, M. S. Rudner, G. Refael, and N. H. Lindner, *Phys. Rev. B* **97**, 245401 (2018).
- [53] N. H. Lindner, G. Refael, and V. Galitski, *Nat. Phys.* **7**, 490 (2011).
- [54] X. Andrade *et al.*, *Phys. Chem. Chem. Phys.* **17**, 31371 (2015).
- [55] A. Castro, H. Appel, M. Oliveira, C. A. Rozzi, X. Andrade, F. Lorenzen, M. A. L. Marques, E. K. U. Gross, and A. Rubio, *Phys. Status. Solidi. B* **243**, 2465 (2006).
- [56] M. A. L. Marques, A. Castro, G. F. Bertsch, and A. Rubio, *Comput. Phys. Commun.* **151**, 60 (2003).
- [57] J. P. Perdew, K. Burke, and M. Ernzerhof, *Phys. Rev. Lett.* **77**, 3865 (1996).
- [58] S. Meng and E. Kaxiras, *J. Chem. Phys.* **129**, 054110 (2008).
- [59] O. Sugino and Y. Miyamoto, *Phys. Rev. B* **59**, 2579 (1999).
- [60] G. F. Bertsch, J. I. Iwata, A. Rubio, and K. Yabana, *Phys. Rev. B* **62**, 7998 (2000).